NEUROPHOTONICS

RESEARCH PAPER

Microprisms enable enhanced throughput and resolution for longitudinal tracking of neuronal ensembles in deep brain structures

Madelyn M. Hjort,[a,b,†] Raajaram Gowrishankar,[b,†] Lucy Tian,[a,b] Adam Gordon-Fennell,[b] Vijay M. K. Namboodiri,[b,‡] Michael R. Bruchas,[a,b] and Garret D. Stuber[a,b,*]

[a]University of Washington, Graduate Program in Neuroscience, Seattle, Washington, United States
[b]University of Washington, Center for the Neurobiology of Addiction, Pain, and Emotion, Department of Anesthesiology and Pain Medicine, Department of Pharmacology, Seattle, Washington, United States

ABSTRACT. **Significance:** Microprism-mediated calcium imaging of deep brain structures allows for reliable tracking of thousands of cells across days, a marked improvement compared with industry-standard approaches utilizing gradient-index (GRIN) lenses.

Aim: We aim to develop a method to record, track, and functionally characterize thousands of cortical and subcortical neurons using an endoscopic microprism and to benchmark the performance against traditional GRIN lenses.

Approach: To improve the visualization throughput of subcortical ensembles, we developed and characterized a protocol to implant a microprism. We performed two-photon calcium imaging through microprisms and compared the yield, cell quality, and optical characteristics to industry-standard GRIN lenses.

Results: We found that our microprism method can stably isolate and track thousands of active neurons across days to weeks. This high-throughput calcium imaging approach facilitates longitudinal functional characterization of large groups of neural ensembles *in vivo* in cortical and subcortical brain structures. This method produces high fidelity trackable cells with superior resolution quality and higher spatial precision when compared with industry-standard GRIN lenses.

Conclusions: The microprism technique represents a significant improvement in throughput and resolution to functionally characterize neuronal ensemble dynamics within deep brain tissues.

Keywords: multi-photon calcium imaging; microprism; longitudinal tracking

Paper 23084SSR received Oct. 6, 2023; revised Feb. 6, 2024; accepted Feb. 13, 2024; published Mar. 20, 2024.

1 Introduction

Understanding how neural ensemble dynamics evolve over time is crucial for grasping the mechanisms of neural and behavioral processes. Longitudinal identification of single cells profiled during these processes using activity alone is challenging when neural activity is anticipated

*Address all correspondence to Garret D. Stuber, gstuber@uw.edu

†These authors contributed equally

‡Current: Department of Neurology, Weill Institute for Neuroscience, Kavli Institute for Fundamental Neuroscience, Center for Integrative Neuroscience, University of California San Francisco, San Francisco, California, United States

to change over time. To address this, optical imaging approaches, such as those capturing calcium-induced fluorescence changes, align cell morphology and field position instead of activity to consistently track cell activity over days to weeks. A prominent optical method that both visualizes and records cellular activity is fluorescence microscopy of genetically encoded voltage, neuromodulator, or calcium indicators, such as GCaMP.[1] Because somatic calcium influx occurs coincident with neural action potentials,[2] the rise in GCaMP fluorescence can serve as an indicator for neural activity. In addition, this fluorescence can be averaged throughout a session to capture a spatial "footprint" of the cells within the field of view (FOV).[1]

The voltage, neuromodulator, and calcium indicators can be excited by either single or multiphoton wavelengths of light.[1] Notably, multiphoton imaging results in sharper cell FOVs, typically facilitating more accurate cell tracking. However, a limitation of two-photon microscopy is its shallow penetration depth; it can only reach a few hundred microns from the brain surface, restricting visualization to the upper cortical layers without additional tradeoffs including reduced resolution and yield[3] or use of hyper-specialized dyes[4] or equipment.[5–7]

Several approaches have been developed to circumvent this limitation, most popularly using a gradient-index (GRIN) lens chronically implanted above the population of interest to relay multiphoton excitation deep into the brain.[8–12] As GRIN lenses employ continuous changes in the refractive index across the lens to focus samples from one end of the lens to the other, relatively minor changes in microscope working distance (WD) can translate to an accurate focus of cell populations even if they are deep within the brain.[10] These benefits are not without their tradeoffs, namely non-uniform excitation and fluorescence collection within the FOV and notable warping in visualized cellular morphology around the lens periphery.[13] Recently, the use of microprisms has emerged as an alternative to GRIN lenses for two-photon imaging in the cortex and superficial hippocampus.[14–17] Because microprisms utilize linear optics, excitation and morphology visualization are uniform across the FOV, but microscopes must be able to travel the microprism length to visualize the population of interest without colliding with the microprism or head-fixation device. Given the limited WD of objectives for standard microscopy, microprisms have been somewhat incompatible for imaging below the superficial cortical surface, leaving many brain structures out of reach. However, recent advances in microscope objective development have produced objectives with compatible WDs (20 mm) for subcortical microprism imaging.[18] Here, we detail and characterize a protocol for imaging the deep brain using microprisms, affording stable, longitudinal tracking of neuronal activity across multiple days over a large FOV. Altogether, this microprism two-photon imaging approach represents a substantial increase in the resolution and throughput of trackable cells over days to weeks.

2 Methods

2.1 Mice

All cortical GRIN and microprism imaging took place in C57BL6/J (7) or CaMKIIa-tta x Teto-GCamp6s (1) mice. DS microprism imaging occurred in D1-cre x Ai14 mice (4), and VS microprism imaging occurred in Vgat-Cre mice. All procedures outlined were approved by UW IACUC (Protocol # 4450-01). See Legaria et al.[19] for additional details for DS GRIN lens mice; in brief, Drd1-cre x Ai14 mice (4) were injected with AAV2/9-CaMKII-GCaMP6s and implanted with a 1×4 mm GRIN lens.[19]

2.2 Microprisms

All microprisms were manufactured by and purchased from OptoSigma. The $1.5 \times 1.5 \times 3$ mm microprisms used for cortical imaging are the same as reported by Spellman et al.[16] (OS PN 160712BK01), whereas the $1.5 \times 1.5 \times 8$ mm microprisms were custom designed (OS PN 22031003567). To facilitate easier implantation of the cortical prisms and to provide a larger surface area for glue, we attached the $1.5 \times 1.5 \times 3$ mm prisms to an 8 mm #1 coverslip (Harvard Apparatus 64-0701) using optical glue (NOA68) applied via a 50cc syringe. As NOA68 is viscous and difficult to load into the syringe, we removed the plunger, squeezed about 0.1 mL into the syringe in the space vacated by the plunger, and then reinserted the plunger to apply one drop of glue to the coverslip. We also attached the coverslip to a metal head-fixation ring.[20] Because our $1.5 \times 1.5 \times 8$ mm microprisms had sufficient surface area above the skull to

apply glue, we omitted the coverslip in preparations involving that implant. We suggest leaving at least 2 mm of additional microprism length above the surface of the brain to allow for adequate fixation to the skull for any custom designs.

2.3 Surgical Preparation

We performed surgery following our previous protocol[21] with the following modifications (see Fig. 1). Please refer to Resendez et al.[21] for more information on the specific surgical equipment, viral dilution testing, and simple troubleshooting steps. A more detailed protocol for this specific surgery, including images, is available upon reasonable request.

We induced anesthesia with 5% isoflurane, headfixed mice on a stereotax, and maintained anesthesia with <1.5% isoflurane. Anesthesia was verified by the lack of a toe pinch response.[21] We performed an incision with surgical scissors or a #10 scalpel blade to expose the skull. Once the surface of the skull was exposed [Fig. 1(a)], we marked the corners of our square craniotomy by gently touching the stereotax-mounted drill bit to the surface of the skull. Refer to Table 1 for "craniotomy corners." We also drilled pilot holes for #00-90 skull screws (B010MMSJJO, Amazon) located over the cerebellum (2×) and olfactory bulb (1×).

We hand-drilled our craniotomy until the drilled bone easily flexed when we gently tapped on the center piece of bone. Following the application of sterile saline, we removed the center bone piece using #5 forceps [Fig. 1(b)]. After extracting any bone shards, we applied a hemostatic sponge (Goodwill AGS111) pre-wetted with sterile saline to control any remaining bleeding. We then inserted skull screws into the drilled pilot holes [Fig. 1(c)]. If the dura did not release when the craniotomy was exposed, we made a superficial incision using a microscalpel (Graham-Field 2979#30) and carefully removed it using a micro curette (FST 10080-05) [Fig. 1(d)]. We applied an additional saline-wetted hemostatic sponge to control bleeding if necessary.

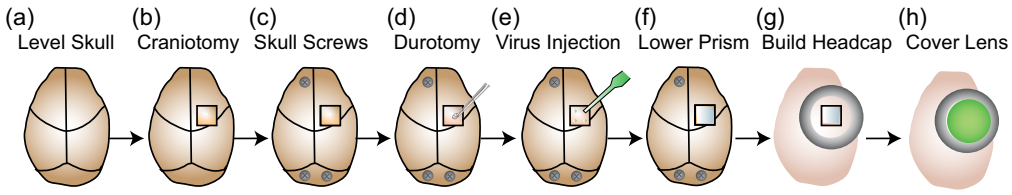

Fig. 1 Surgical implantation of microprism. Schematic of major surgical steps. (a) Begin with a cleaned, leveled exposed skull. (b) Craniotomy with the central skull piece removed. (c) Insertion of skull screws for headcap stability. (d) Durotomy with microcurette. (e) Injection of virus into the craniotomy. (f) Microprism lowered through craniotomy into the target brain area. (g) Microprism secured to the skull with superglue and dental cement. (h) Final preparation with microprism, headring, headcap, and protective covering. A detailed protocol with images is available upon request.

Table 1 Surgical coordinates.

Microprism	Location	Craniotomy corners	Virus injections	Microprism corner
1.5 × 1.5 × 3	Prefrontal cortex	AP 1.85 and 3.60	AP 1.94	AP 2.05
		ML 0.25 and 2.00	ML 0.75 and 1.25	ML 0.3
			DV −2.25 and −1.85	DV −2.5
1.5 × 1.5 × 8	Dorsal striatum	AP 0.0 and 1.75	AP 0.5 and 1.5	AP 0.25
		ML 2.0 and 0.25	ML 1.65	ML 1.75
			DV −3.25 and −3.0	DV −3.5
1.5 × 1.5 × 8	Ventral striatum	AP −0.3 and 2.3	AP 0.85 and 1.50	AP 0.65
		ML 1.65 and 3.3	ML 1.65	ML 1.75
			DV −4.0 and −3.25	DV −4.25

For prefrontal cortex surgeries, we injected 4×400 nL of AAVDJ-CaMKIIa-GCaMP6s (UNC Vector Core lot av6364) at the locations indicated in Table 1. Mice for experiments shown in Fig. 4 received a 3:1 mix of GCaMP6s and AAV8-CAMKIIa-ChRmine.[22] For striatal surgeries, we injected 4×300 nL of AAVDJ-hSyn-GCaMP6s (Stanford Vector Core) at the locations indicated in Table 1. All injections were performed using a Nanoject II (Drummond) at a rate of 1 nL/s. For injections performed at the same ML coordinates, we did not pause between the ventral and dorsal injections, but waited at least 15 min between the dorsal injection and removal of the glass pipette from the brain [Fig. 1(e)].

Following all virus injections, the brain surface was cleaned until it was free of active bleeds and/or blood clots near the site of the microprism face implant. Active bleeding or blood clots

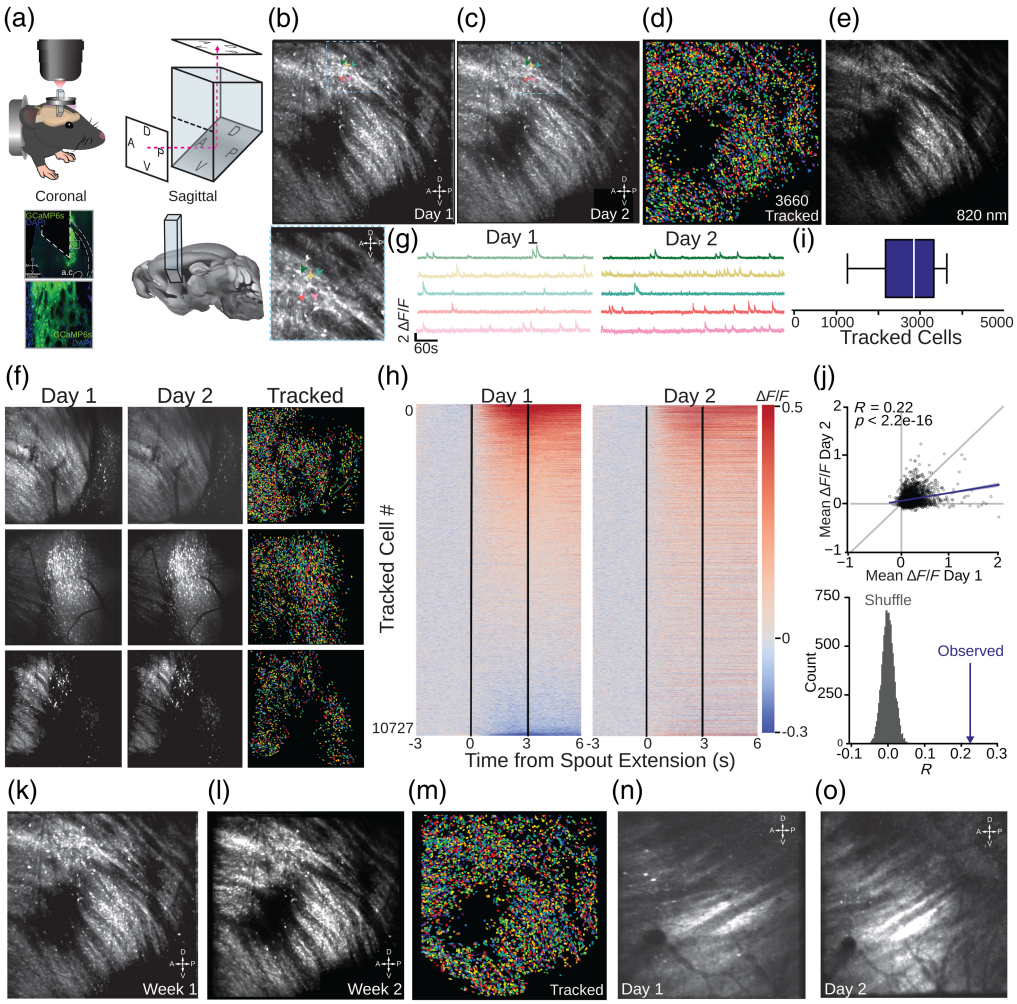

Fig. 2 Visualization of the DS and VS with the microprism approach. (a) 3D rendering of prism in mouse brain, imaging plan transformation through prism, and track schematics on sagittal sections adapted from Allen CCF, and coronal histological section (10× upper, 40× lower, showing implant track, GCaMP6s and DAPI). (b) (Upper) Sample FOV for representative mouse on day 1; (lower) higher-resolution zoom with cells indicated. (c) Sample FOV for representative mouse on day 2. (d) Tracked ROIs from (b) and (c). (e) Registration plane at 820 nm for activity-independent tracking. (f) Tracked FOVs from additional mice. (g) Sample extracted transients for DS cells on days 1 (left) and 2 (right). Cells are marked in (b)–(c). (h) Peri-stimulus time histograms of the spout retraction/sucrose-delivery aligned activity from all mice on days 1 (left) and 2 (right). Vertical lines indicate the spout extension and retraction. (i) Quantification of cells tracked across days in the DS in one FOV for four mice (b)–(d), (f). (j) Correlation analysis of mean fluorescence in (h) during access period (0 to 3 s) across days. (k) (b) reproduced. (l) FOV from B/K tracked over 2 weeks. (m) Extracted masks from tracking of (k) and (l) (3726 cells). (n) Sample VS FOV on day 1. (o) Sample VS FOV on day 2 (Video 1, MOV, 5.89 MB [URL: https://doi.org/10.1117/1.NPh.11.3.033407.s1]).

near the implant site can travel with the microprism to the imaging FOV and cause obstructions. Aspiration or pre-lowering of a needle into the craniotomy was not necessary for any of our applications, and we did not observe obvious indicators of tissue compaction in post-recording histology [Fig. 2(a)].

We held the $1.5 \times 1.5 \times 8$ mm microprism with a surgical bulldog clamp (WPI 14119) covered with heat shrink tubing (Qualtec Qkit 1) on a stereotaxic electrode holder (Kopf, Model 1773). We held the $1.5 \times 1.5 \times 3$ mm microprism apparatus using a miniscope clamp (Inscopix), though other methods are also likely viable.

We measured our microprism implant coordinates at Bregma from the medial caudal corner of the microprism, as we found this easiest to visualize and reliably locate. After positioning the microprism over the desired implant site, we removed any remaining hemostatic sponge, applied additional saline, and lowered the microprism at a maximum of 500 μm/ min [Fig. 1(f)]. If any profuse bleeding occurred, we removed the microprism, stopped the bleeding, and reinserted the microprism.

Once the microprism was at the desired coordinates, we glued (Loctite 234790) it in place and cured the glue using a dental cement activator (Jet 1406). We then removed the lowering clamp and added a layer of C&B Metabond (Parkell S380) to further affix the implant on the skull. Successful implants allow for visualization of brain tissue through the implant.

For $1.5 \times 1.5 \times 8$ mm implants, we lowered a metal headring (see Gordon-Fennell et al.[20] for narrow sidewall.stl file) around the implant, ensuring that the microprism was slightly recessed by creating a superglue platform to rest the headring as needed. We then secured the headring to the skull using dental cement (Jet 1230-P). To better identify animals, we wrote a number into the dental cement when mostly dry using a permanent marker (Sharpie 1735792) [Fig. 1(g)]. We protected the microprism by covering it with silicone sealant (WPI KWIK-CAST) [Fig. 1(h)]. Animals recovered for at least 2 weeks before initial FOV visualization, and at least 4 weeks before experiments began.

2.4 *In-Vivo* Imaging and Tracking of Neurons Visualized through Microprisms

We performed all $1.5 \times 1.5 \times 8$ mm microprism imaging on a Bruker Investigator two-photon microscope through a Cousa objective (20 mm WD).[18] All $1.5 \times 1.5 \times 3$ mm microprism were imaged on an Olympus FVMPE-RS with an XLPLN10xSVMP (NA0.6, 8 mm WD) immersion objective except for the point spread function (PSF) and stimulation data, which took place on a Bruker2p+ using the Cousa and TL10X-2P objectives, respectively, and all cortical GRIN lens imaging on a Bruker 2p+ though a TL10X-2P (NA 0.5, 8 mm WD) objective. On Bruker microscopes, we imaged with an InSight X3 laser at 820 nm for plane registration and 920 nm for functional GCaMP imaging. Olympus microscopes utilized a MaiTai DeepSee laser at the same wavelengths. All data were acquired at 7.5 Hz on resonant galvos (four frame averaging). All GRIN and prefrontal cortical (PFC) microprism data were acquired at 512×512 pixel resolution, whereas DS and VS microprism data were collected at 1024×1024, which allowed for a higher quality signal in the extracted transients. The DS GRIN dataset in Fig. 3 was used with permission from the authors of Legaria et al.[19] and was collected using a N16XLWD-PF (0.8 NA, 3 mm WD) objective at 30 Hz. The PFC GRIN lens dataset used in Fig. 3 was previously published by our group.[23]

We used an open-source head-fixed rodent behavioral experimental training system (OHRBETS)[20] for all $1.5 \times 1.5 \times 8$ mm microprism imaging. To facilitate better leveling of the imaging plane, we mounted the OHRBETS stage on a Thorlabs goniometer platform (TTR001/M). We verified that the microprism was level in three ways. First, after cleaning the microprism of debris on a dissecting microscope, we adjusted the goniometer until the light of the microscope illuminated the microprism evenly (white). Second, when visualizing the microprism using the eyepieces of the two-photon microscope, we ensured that all four corners were even and sharply in focus. Third, we ensured a uniform laser flare on the microprism face before lowering the objective to the imaging plane. Imaging with the microprisms, as with GRIN lenses, is possible without the goniometer stage, but in our experience, it often has a dimmer, lower yield FOV and impaired tracking across days. To register a consistent imaging plane across days, we first imaged at 820 nm [Fig. 2(b)], the approximate isosbestic wavelength at which GCaMP6 is equally fluorescent calcium free and calcium bound.[24] Because this image was independent of the activity

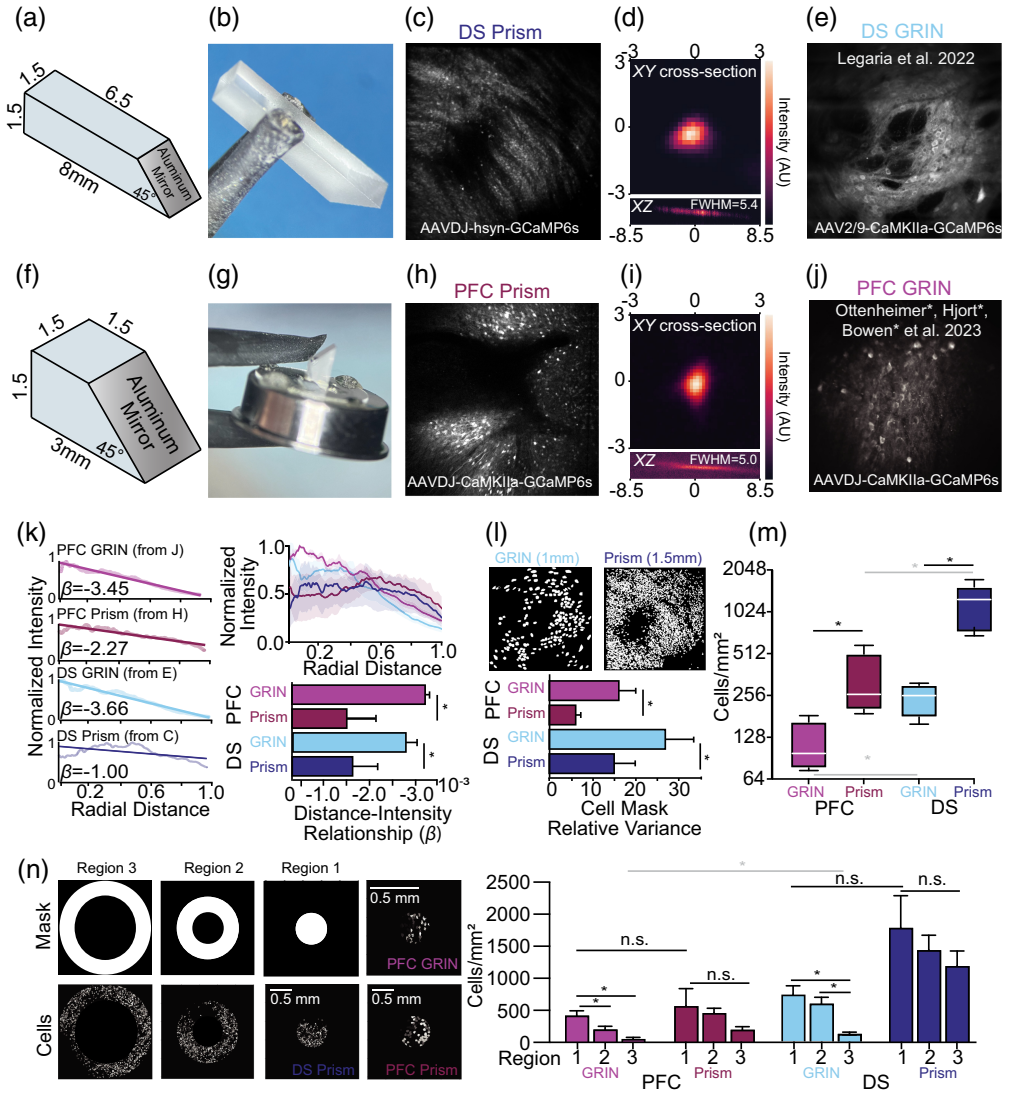

Fig. 3 Optical properties of microprism preparations and comparison with field standard GRIN lens preparations. (a) Schematic of $1.5 \times 1.5 \times 8$ mm microprism. (b) Photo of $1.5 \times 1.5 \times 8$ mm microprism. (c) Sample FOV from GRIN microprism PFC prep. (d) PSF for $1.5 \times 1.5 \times 8$ mm microprism of 100 nm bead. (e) Sample FOV from GRIN lens DS prep, reproduced from Jung et al.[12] with permission. (f) Schematic of $1.5 \times 1.5 \times 3$ mm microprism (from Meng et al.[10]). (g) Photo of $1.5 \times 1.5 \times 3$ mm microprism. (h) Sample FOV from microprism PFC prep. (i) PSF for $1.5 \times 1.5 \times 3$ mm microprism of 100 nm bead. (j) Sample FOV for GRIN PFC prep. (k) (Left) Intensity-distance relationships for example FOVs in (c), (d), and (h), (i). (Right, upper) Measurement of normalized intensity (% of maximum) from center of lens FOV for PFC GRIN (magenta), PFC prism (maroon), DS GRIN (cyan), and DS prism (indigo) preparations. Mean ± SEM. (Right, lower) The relationship between the distance and intensity (slope of linear fits from k, left) is significantly stronger for GRIN lenses compared with prisms in both the PFC and DS [two-way ANOVA, brain area: $F(1,12) = 0.0708$, implant type: $F(1,12) = 9.2387$, $p = 0.01028$, interaction: $F(1,12) = 0.4768$]. (l) (Upper) Visualization of cell masks for DS GRIN lens (left, from c) and prism (right, from d). (Lower) Quantification of relative variance (variance divided by mean to account for different mask size in imaging fields) for GRIN and prism FOVs in DS and PFC. Masks vary more significantly in size in GRIN compared with prism lens preparations. Two-way ANOVA, brain area: $F(1,12) = 4.7125$, implant type: $F(1,12) = 5.8072$, $p = 0.03292$, interaction: $F(1,12) = 0.0491$. (m) Cell density of GRIN and prism preparations. There is a significant difference between GRIN and prism cell density in PFC and DS, as well as a difference in the number of cells visualized between regions. Two-way ANOVA, brain area: $F(1,12) = 18.13$, $p = 0.0011$, implant type: $F(1,12) = 24.07$, $p = 0.0004$, interaction: $F(1,12) = 10.10$, $p = 0.0080$. (n) Quantification of cell density across distance from center of GRIN or microprism. Mean ± SEM. There is not a significant

Fig. 3 (*Continued*) difference between cell densities at FOV center across GRIN and microprism. Two-way ANOVA, brain area: $F(1,12) = 6.973$, $p = 0.02155$, implant type: $F(1,12) = 4.24$, $p = 0.06$, interaction: $F(1,12) = 2.4096$, $p = 0.1466$, though intensity decreases with distance for GRIN lenses in the PFC [one-way RM ANOVA, $F(2,3) = 14.6647$, $p = 0.001473$] and DS [$F(2,3) = 11.7578$, $p = 0.003088$]. For all comparisons, asterisk = significance at $\alpha < 0.05$.

state of the system, we used 820 nm acquired images to compare resolvable cells across multiple daily imaging sessions during data acquisition.

Following recording, we tracked imaged cells over days by concatenating all imaging sessions and running them through Suite2p.[25] This both corrected motion within days and small misalignments across days with some modifications from the default. In brief, enabling two_step_registration = 1, increasing the snr_threshold (to 2), and increasing maxregshiftNR (to 50) improved automated cross-day registration. We manually verified cells as tracked (i.e., sorted to "cells") if they had at least one visible transient each recording day.

2.5 Data Analysis

2.5.1 *Peri-event time histogram creation*

Following motion correction, we standardized the fluorescence between cells by subtracting and subsequently dividing by the mean of each trace over the entire session. We then generated peri-event time histograms of our data for Fig. 2(h).

2.5.2 *Field of view quality*

To quantify variations in field fluorescence between the GRIN lens and microprisms, we averaged pixel fluorescence in concentric circles from the FOV center. We fit the resulting measurement with a linear model to quantify the relationship between field fluorescence and the distance from the center of the imaging field and used the slope (β) to compare this relationship between recording methods.

2.5.3 *Cell mask variance and counts*

We isolated the cells within our FOV using Suite2p for PFC GRIN and DS microprism imaging and manually for PFC microprism and DS GRIN imaging. We then calculated the area of each mask using custom python scripts. To compare variations in the mask size (with the goal of highlighting irregular and stretched cells around the GRIN lens periphery), we calculated the variance of these area measurements and divided by the mean mask size to standardize across cells of different sizes in PFC and DS GRIN and microprism preps. We also compared the total number of cells visualized in each preparation per unit implant area and quantified the relationship between cell density and distance from implant center in three concentric circles. All statistical testing utilized balanced two-factor ANOVA with replication to compare brain areas (PFC and DS) and implant types (GRIN or prism) or one-way RM ANOVA within a single area, both at $\alpha < 0.05$ (Table S1 in the Supplementary Material). All analysis scripts are available on request.

2.6 Microprisms for Spatial Light Modulation Applications

We assessed the suitability of microprisms for single cell stimulation and characterized the PSF of the microprisms following previous methods.[26] All statistical testing utilized repeated measures one-way ANOVA with Tukey honest significant difference test comparing all columns to 0 offset at $\alpha < 0.05$.

3 Results

To determine the capabilities of $1.5 \times 1.5 \times 8$ mm microprisms, we implanted the microprism into the dorsal striatum (DS), a subcortical region important for reward processing and movement

[Fig. 2(a)]. After mice recovered from surgery, we leveled the microprisms for imaging (see Sec. 2) and used the long WD Cousa 10× objective[18] to descend to the focal plane above the neurons that we aimed to visualize [Figs. 2(b)–2(e)]. Manual alignment under the microscope and automated registration allowed for tracking cells in the DS across multiple days [Figs. 2(b)–2(d); Video 1] even though mice were returned to their home cages at the end of each recording session. We visualized a total of 10,727 stable and trackable cells with this preparation, with 2681 ± 516 (mean $\pm$ SEM) trackable cells per FOV in each of four mice [Figs. 2(b)–2(d), 2(f), and 2(i)]. Extracted activity demonstrates that neurons were active and dynamic on all recording days [Figs. 2(g) and 2(h)]. When aligned to spout extension and sucrose delivery, many cells show a robust increase in activity that is consistent across days [Figs. 2(h)–2(j)]. Notably, most of these neurons are also trackable over multiple weeks [Figs. 2(k)–2(m)]. We also implanted the ventral striatum (VS) using the same method, and we were able to visualize trackable cells within an imaging plane [Figs. 2(n)–2(o)]. Taken together, these results illustrate the utility of our preparation for functional, longitudinal imaging of subcortical neural populations.

To characterize the optical quality of our microprism imaging method [Figs. 3(a)–3(d)], we compared it with a published preparation[16] utilizing a microprism for functional characterization of PFC ensembles [Figs. 3(f)–3(i)]. Both preparations have high-quality lateral resolution (~2 μm) that is much lower than the average diameter of neurons in our preparations (~20 μm) [Figs. 3(d), 3(i), and 4(d)], which suggests that they may be useful for studying some subcellular processes, though we did not test this directly. On average, we visualized 730 ± 201 PFC and 2781 ± 505 DS neurons in each microprism preparation on a single day (mean $\pm$ SEM) [Fig. 3(m)]. Given the high level of spatial specificity that we can achieve with this

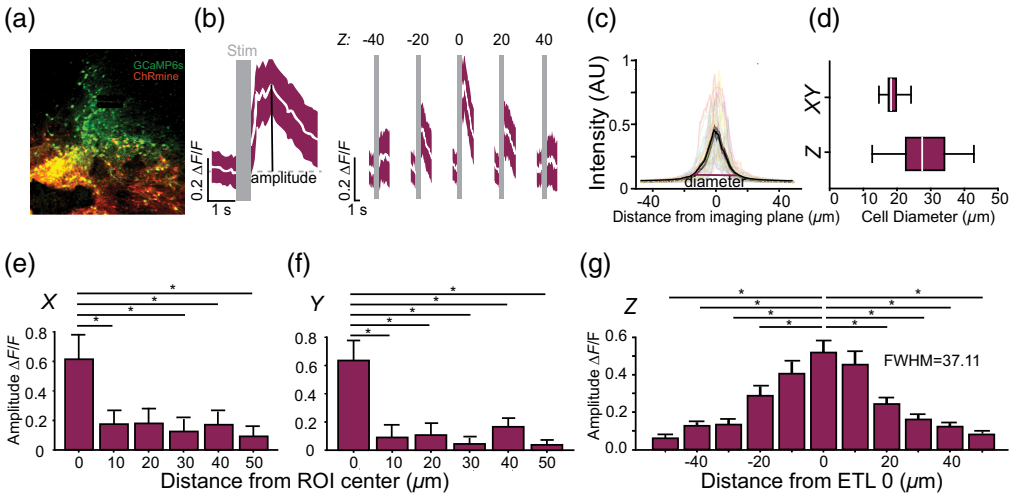

Fig. 4 Characterizing microprism suitability for single cell stimulation. (a) Sample FOV through PFC prism using TL10x. (b) (Left) Sample evoked transient with the stim period and amplitude measurement used for (e)–(g) indicated. (Right) Sample stim response at ±0, 20, and 40 μm. White mean ± magenta SEM. (c) *Z*-stack through stimulation ROIs [from (g)] to quantify cell diameter, 95% of peak width indicated and was used for (d). (d) Quantification of cell dimensions for lateral (*XY*) and axial (*Z*) resolutions. (e) Average evoked signal from stimulation ROI offsets in *X* plane in increments of 10 μm for 30 cells from three animals. Asterisks indicate significant differences from approximate cell centroid at $\alpha < 0.05$ in one-way repeated measures ANOVA with Tukey HSD test. *X*: $F(5,95) = 2.9758$, $p = 0.01538$; 0 to 10, $p = 0.03371$; 0 to 20, $p = 0.1075$; 0 to 30, $p = 0.01084$; 0 to 40, $p = 0.03373$; 0 to 50, $p = 0.0076534$. (f) Like (e) but in *Y* plane. *Y*: $F(5,95) = 10.4351$, $p = 0.000448$; 0 to 10, $p = 0.003537$; 0 to 20, $p < 0.0001$; 0 to 30, $p = 0.001098$; 0 to 40, $p = 0.005559$; 0 to 50, $p = 0.0004289$. (g) Average evoked signal from stimulation ROI offsets in *Z* plane in increments of 10 μm for 30 cells from three animals [see (b)]. Asterisks indicate significant differences from ETL 0 at $\alpha < 0.05$ in one-way repeated measures ANOVA with Tukey HSD test. *Z*: $F(29,290) = 17.81$, $p < 0.0001$; 0 to −50, $p < 0.0001$; 0 to −40, $p < 0.0001$; 0 to −30, $p < 0.0001$; 0 to −20, $p = 0.0263$; 0 to −10, $p = 0.4793$; 0 to 10, $p = 0.6582$; 0 to 20, $p = 0.0011$; 0 to 30, $p = 0.0001$; 0 to 40, $p < 0.0001$; 0 to 50, $p < 0.0001$.

preparation, it will be suitable to image most neuronal cell types in the brain regions reachable with these prisms.

We also compared our microprism recordings with those using industry-standard 1×4 mm GRIN lenses [Figs. 3(e) and 3(j)] with comparable objectives and zoom (see Sec. 2). Both GRIN lens datasets were sourced from recent literature from our (PFC) and other (DS) groups.[19,23] The microprisms facilitate a statistically significant decrease in the relationship between radial distance from the lens center and fluorescence, indicating a more uniform brightness across the FOV [Fig. 3(k)]. Microprisms also produce more consistently sized cell masks [Fig. 3(l)]. On average, we were able to visualize hundreds of cells through GRIN lenses over a 0.785 mm^2 surface and thousands of cells across a single plane in our microprism preparation over a 2.25 mm^2 surface [Fig. 3(m)]. We also evaluated the relationship between cell density and distance from the center of the imaging field in GRIN and microprism preparations. Notably, there is not a significant difference in cell density at the center of GRIN and microprism preparations, though cell density significantly decreases with distance from the center in GRIN recordings [Fig. 3(n)]. These results indicate that this approach produces a marked improvement in FOV quality and neuron yield in microprism preparations compared with GRIN lens imaging.

Finally, we characterized the suitability of microprism preparations for single cell optogenetics using a spatial light modulator to activate the two-photon compatible opsin, ChRmine[22] [Fig. 4(a)]. The lateral resolution within the visualized plane was within the diameter of a single cell [Figs. 4(d)–4(f)], whereas the axial (Z) resolution was only slightly larger than the diameter of the imaged cells in the Z-dimension [Figs. 4(c), 4(d), and 4(g)]. This physiological resolution will further depend on opsin and other biological factors in additional preparations. Notably, we did not observe any cells with a vertical alignment [as would appear by additional peaks in Fig. 4(c)] such that this poorer z-resolution would stimulate off target cells. Taken together, these results suggest that microprism preparations can be used to both read neural activity and perform holographic spatial light modulation for single cell optogenetics with a higher throughput.

4 Discussion

Here, we present a high cell yield imaging approach to visualize deep regions of the brain via two microprisms (3 and 8 mm in length). Compared with commonly used GRIN lens approaches, the microprism preparation (Fig. 1) provides a ~10× increase in cell yield, a more uniform FOV visualization, and a much larger FOV (Fig. 3). Using these microprisms, we were able to track thousands of dynamic neurons across days within a single FOV in the DS, which can be aligned to task events and further analyzed (Fig. 2). This microprism-mediated preparation achieves the necessary optical resolution for cellular—and perhaps subcellular—imaging (Fig. 3). Stable FOVs can be tracked over multiple sessions (Fig. 2) and stimulated using optogenetics (Fig. 4). Altogether, this technique provides a marked improvement upon canonical preparations to visualize and track single cells in deeper brain structures.

Although the Cousa objective has a larger FOV that could account for differences in cell density yield between GRIN and microprism recordings, it is unlikely that it is the main driver of this effect. Moreover, the periphery of the GRIN lens recordings [Figs. 3(e) and 3(j)] already display substantial aberrations and limited resolvable ROIs. Increasing the imaging FOV is unlikely to resolve these aberrations that are inherent to the GRIN lens preparation. Furthermore, the increased yield is not attributable only to differences in microprism and GRIN size, as both PFC and DS microprism preparations have a higher density of cells per squared millimeter [Fig. 3(m)]. Likewise, it is unlikely that there are substantial axial resolution differences that account for the differences that we observed. Cell density yield between GRIN and microprism preparations did not significantly differ at the center of the imaging field [Fig. 3(n)] and the physiological axial resolution for microprisms [Fig. 4(g)] is comparable to published literature measurements for GRIN lenses on the same microscope.[26] Our results [Fig. 3(n)] suggest that this differential yield is attributable to a significant reduction in the density of resolvable cell ROIs near the edges of GRIN lens preparations. Although differences in implant size, microscopes objectives used, or axial resolution could impact the total cell number, our results suggest that the improved optics of the microprism, including its more uniform FOV, drive the improvements in cell density that we report.

The length of our implant is sufficient to image at any depth in the mouse brain, though its large footprint may certainly limit its suitability for some areas. We chose to fabricate a single size that was feasible for recording in any area to allow for ordering in large batches, which in our experience significantly reduces the microprism cost. Other users may consider reducing the implant length according to their needs, though an important consideration is to allow for a sufficient surface area above the brain for gluing or cementing the microprism to the skull if attaching the microprism to a coverslip is undesirable.

This approach can likely be adapted for one-photon miniscope recordings with some modifications to the miniscope apparatus. Because the optics must move a much longer distance to focus down the length of microprisms, compared with GRIN lenses, miniscopes will likely need to adjust the mounting distance between the imaging optics and microprism or the range and position of the internal focus. Ordering microprisms of the correct length for each application, as opposed to a more universal 8 mm length, may help mitigate these risks.

In conclusion, we developed an approach that improves upon canonical approaches to allow for high-quality tracking of thousands of neurons across days in the deep brain.

Disclosures

No conflicts of interest, financial or otherwise, are declared by the authors.

Code and Data Availability

All data and analysis scripts are available from the corresponding author upon reasonable request. Microprisms can be purchased from OptoSigma using OS PN 160712BK01 (3 mm) OS PN 22031003567 (8 mm).

Author Contributions

Conceptualization: MH, GDS, RG, MRB. Methodology: microprism and surgical design- MH and GDS. MH, RG, VMKN, and AGF performed surgeries; MH, LT, and AGF took surgery photos. Investigation: MH [Figs. 2(n)–2(o), 3(h), 3(j), and 4], RG [Figs. 2(b)–2(f), 2(k)–2(m)], LT [Figs. 3(d) and 3(i)]. Data curation: MH, RG. Formal analysis and visualization: MH, AGF [Fig. 2(j)], LT [Figs. 3(d) and 3(i)]. Writing–original draft: MH. Writing–review and editing: MH, RG, AGF, VMKN, GDS, MRB. Funding acquisition: GDS, MH, RG, MRB. Supervision: GDS, MRB. Competing interests: The authors have no competing interests to declare.

Acknowledgments

We would like to thank Alex Legaria, Ben Yang, Alexxai Kravitz, and Jones Parker for sharing their DS GRIN lens dataset for our use in Fig. 3. We would also like to thank Kyle Haddock and colleagues at OptoSigma for microprism design assistance, as well as Charles Zhou for assistance with protocols for optical characterization of the microprisms. We thank Charu Ramakrishnan, Karl Deisseroth, and Larry Zweifel for viral constructs. We would like to thank Sean Piantadosi for comments on this manuscript. This work was supported by F31DA053706 (MH), K99DA059709 (RG), F32 DA054719 (AGF), NSF 1934288 & R37DA032750 (GDS), P30DA048736 (GDS & MRB) and R37DA033396 (MRB), and the Weill Neurohub (MRB).

References

1. T.-W. Chen et al., "Ultra-sensitive fluorescent proteins for imaging neuronal activity," *Nature* **499**, 295–300 (2013).
2. A. L. Hodgkin and A. F. Huxley, "A quantitative description of membrane current and its application to conduction and excitation in nerve," *J. Physiol.* **117**, 500–544 (1952).
3. P. Theer and W. Denk, "On the fundamental imaging-depth limit in two-photon microscopy," *J. Opt. Soc. Am. A* **23**, 3139–3149 (2006).
4. C. H. Tischbirek, A. Birkner, and A. Konnerth, "*In vivo* deep two-photon imaging of neural circuits with the fluorescent Ca^{2+} indicator Cal-590," *J. Physiol.* **595**, 3097–3105 (2017).
5. R. Lu et al., "Video-rate volumetric functional imaging of the brain at synaptic resolution," *Nat. Neurosci.* **20**, 620–628 (2017).
6. M. Yildirim et al., "Functional imaging of visual cortical layers and subplate in awake mice with optimized three-photon microscopy," *Nat. Commun.* **10**, 177 (2019).

7. K. Wang et al., "Direct wavefront sensing for high-resolution *in vivo* imaging in scattering tissue," *Nat. Commun.* **6**, 7276 (2015).
8. Y. Ziv et al., "Long-term dynamics of CA1 hippocampal place codes," *Nat. Neurosci.* **16**, 264–266 (2013).
9. J. M. Otis et al., "Prefrontal cortex output circuits guide reward seeking through divergent cue encoding," *Nature* **543**, 103–107 (2017).
10. G. Meng et al., "High-throughput synapse-resolving two-photon fluorescence microendoscopy for deep-brain volumetric imaging *in vivo*," *eLife* **8**, e40805 (2019).
11. M. J. Levene et al., "*In vivo* multiphoton microscopy of deep brain tissue," *J. Neurophysiol.* **91**, 1908–1912 (2004).
12. J. C. Jung et al., "*In vivo* mammalian brain imaging using one- and two-photon fluorescence microendoscopy," *J. Neurophysiol.* **92**, 3121–3133 (2004).
13. S. Xu et al., "Behavioral state coding by molecularly defined paraventricular hypothalamic cell type ensembles," *Science* **370**, eabb2494 (2020).
14. R. J. Low, Y. Gu, and D. W. Tank, "Cellular resolution optical access to brain regions in fissures: imaging medial prefrontal cortex and grid cells in entorhinal cortex," *Proc. Natl. Acad. Sci. U. S. A.* **111**, 18739–18744 (2014).
15. W. T. Redman et al., "Long-term transverse imaging of the hippocampus with glass microperiscopes," *eLife* **11**, e75391 (2022).
16. T. Spellman et al., "Prefrontal deep projection neurons enable cognitive flexibility via persistent feedback monitoring," *Cell* **184**, 2750–2766.e17 (2021).
17. M. L. Andermann et al., "Chronic cellular imaging of entire cortical columns in awake mice using microprisms," *Neuron* **80**, 900–913 (2013).
18. C.-H. Yu et al., "The Cousa objective: a long working distance air objective for multiphoton imaging *in vivo*," *Nat. Methods* **21**(1), 132–141 (2023).
19. A. A. Legaria et al., "Fiber photometry in striatum reflects primarily nonsomatic changes in calcium," *Nat. Neurosci.* **25**, 1124–1128 (2022).
20. A. Gordon-Fennell et al., "An open-source platform for head-fixed operant and consummatory behavior," *eLife* **12**, e86183 (2023).
21. S. L. Resendez et al., "Visualization of cortical, subcortical, and deep brain neural circuit dynamics during naturalistic mammalian behavior with head-mounted microscopes and chronically implanted lenses," *Nat. Protoc.* **11**, 566–597 (2016).
22. J. H. Marshel et al., "Cortical layer-specific critical dynamics triggering perception," *Science* **365**, eaaw5202 (2019).
23. D. J. Ottenheimer et al., "A stable, distributed code for cue value in mouse cortex during reward learning," *eLife* **12**, RP84604 (2023).
24. L. M. Barnett, T. E. Hughes, and M. Drobizhev, "Deciphering the molecular mechanism responsible for GCaMP6m's Ca^{2+}-dependent change in fluorescence," *PLoS ONE* **12**, e0170934 (2017).
25. M. Pachitariu et al., "Suite2p: beyond 10,000 neurons with standard two-photon microscopy," bioRxiv (2017).
26. S. C. Piantadosi et al., "Holographic stimulation of opposing amygdala ensembles bidirectionally modulates valence-specific behavior via mutual inhibition," *Neuron* **112**, 593–610 (2023).

Biographies of the authors are not available.